Ultrathin films of black phosphorus as suitable platforms for unambiguous observation of the orbital Hall effect

Tarik P. Cysne,[1,*] Marcio Costa,[1] Marco Buongiorno Nardelli,[2] R. B. Muniz,[1,†] and Tatiana G. Rappoport[3,4]
[1]*Instituto de Física, Universidade Federal Fluminense, 24210-346 Niterói, Rio de Janeiro, Brazil*
[2]*Department of Physics and Department of Chemistry, University of North Texas, Denton, Texas 76203, USA*
[3]*Centro de Física das Universidade do Minho e do Porto (CF-UM-UP) e Departamento de Física, Universidade do Minho, P-4710-057 Braga, Portugal*
[4]*Instituto de Física, Universidade Federal do Rio de Janeiro, C.P. 68528, 21941-972 Rio de Janeiro, Rio de Janeiro, Brazil*

(Received 1 August 2023; revised 28 September 2023; accepted 6 October 2023; published 19 October 2023)

Phosphorene, a monolayer of black phosphorus, is a two-dimensional material that lacks a multivalley structure in the Brillouin zone and has negligible spin-orbit coupling. This makes it a promising candidate for investigating the orbital Hall effect independently of the valley or spin Hall effects. To model phosphorene, we utilized a density-functional-theory-derived tight-binding Hamiltonian, which is constructed with the pseudoatomic orbital projection method. For that purpose, we use the PAOFLOW code with a newly implemented internal basis that provides a fairly good description of the phosphorene conduction bands. By employing linear response theory, we show that phosphorene exhibits a sizable orbital Hall effect with strong anisotropy in the orbital Hall conductivity for the out-of-plane orbital angular momentum component. The magnitude and sign of the conductivity depend on the in-plane direction of the applied electric field. These distinctive features enable the observation of the orbital Hall effect in this material unambiguously. The effects of strain and of a perpendicularly applied electric field on the phosphorene orbital Hall response are also explored. We show that a supplementary electric field applied perpendicular to the phosphorene layer in its conductive regime gives rise to an induced in-plane orbital magnetization.

DOI: 10.1103/PhysRevB.108.165415

I. INTRODUCTION

The phenomenon known as the orbital Hall effect (OHE) is characterized by the emergence of an orbital angular momentum (OAM) current that flows transversely to the direction of an applied electric field. Distinctly from the spin Hall effect (SHE), the OHE does not require the presence of spin-orbit interaction to occur. Despite being predicted nearly two decades ago [1], the prospect of using the OHE to generate OAM current in certain materials has recently sparked great interest in the solid-state physics community [2–13]. OAM currents can be produced in a wide range of materials, and their intensities can exceed those of spin current. Furthermore, they can be injected into adjacent elements to exert torque on magnetic units, expanding their possible applications in orbitronics [14,15].

As a matter of fact, light metals with weak spin-orbit coupling are being explored as a means of generating orbital currents in three-dimensional metals [16]. Recently, orbital torques have been realized in light metal/ferromagnet heterostructures, providing indirect but robust experimental evidence of the OHE [17–19].

The OHE has also been investigated in two-dimensional (2D) materials that, in some cases, may host an orbital Hall (OH) insulating phase, characterized by a finite OH conductivity plateau located within the insulating band gap [20,21]. Recent studies have shed light on the fascinating properties of the OH insulating phase in these materials, such as its connection with higher-order topological phases [22] and the encoding of nontrivial topology associated with OAM in an orbital Chern number [23,24].

The difficulty in discerning the OHE from other angular momentum transport phenomena has hindered its unequivocal direct observation. For example, in some cases the spin accumulation produced by the spin Hall effect may be hard to distinguish from its orbital angular momentum counterpart. The valley Hall effect (VHE) induced by a longitudinally applied electric field that occurs in noncentrosymmetric lattices with multivalley structure in the Brillouin zone involves the transverse flow of valley currents that may also carry magnetic moment [23–26], which can be hard to dissociate from the intra-atomic orbital Hall contribution.

Multiorbital 2D materials possess natural symmetry constraints that lead to various types of orbital hybridization, which can maximize the OHE [22]. However, to single out the OHE unequivocally, it is crucial to identify materials with weak spin-orbit coupling that display no significant spin Hall effect (SHE) and no VHE or magnetoelectric effects that may mask the OHE.

In this paper, we suggest that phosphorene is a very suitable material for directly observing the OHE in 2D materials. It is a centrosymmetric semiconductor with a sizable direct band gap

*tarik.cysne@gmail.com
†bechara@if.uff.br

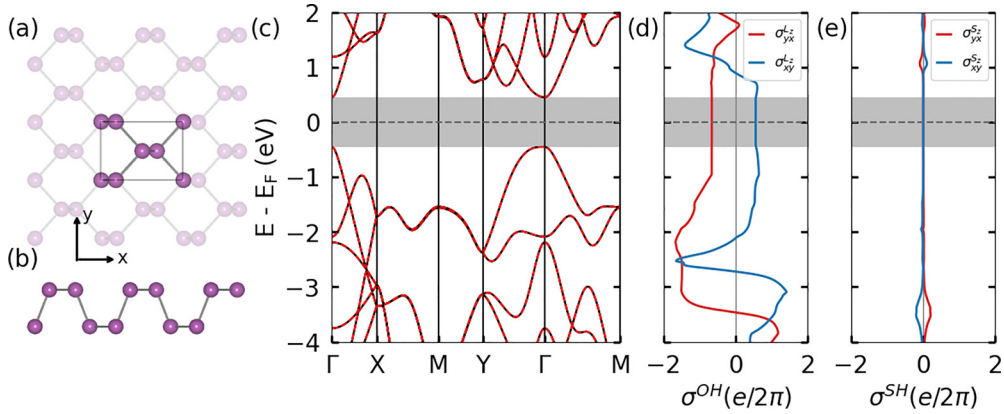

FIG. 1. Phosphorene crystal structure (a) top and (b) side views. (c) Band structure: DFT (solid black curve) and PAOFLOW (dashed red curve). (d) and (e) Orbital Hall (OH) and spin Hall (SH) conductivities, respectively, calculated as functions of energy for electric fields applied along the $\hat{x}$ (red) and $\hat{y}$ (blue) directions.

at the Γ point of the 2D Brillouin zone (BZ) [27–31] that does not host a VHE. In the absence of reasonably strong electric fields, applied perpendicularly to the layer, it behaves as an ordinary insulator and shows no spin Hall effect (SHE) within its band gap [32]. The spin-orbit interaction in phosphorene is extremely weak [33,34], and consequently it also displays negligible SHE in the metallic regime in comparison with the OHE, as we shall see later. Symmetry prevents the appearance of the magnetoelectric effect in phosphorene, even in the presence of strain [35].

Here, we have performed density functional theory (DFT) calculations combined with linear response theory to analyze the OH response in phosphorene. Our calculations show that phosphorene exhibits sizable anisotropic OH conductivities that change sign for in-plane electric fields applied along the armchair ($\hat{x}$) and zigzag ($\hat{y}$) Cartesian directions depicted in Fig. 1. These features persist in the presence of moderate in-plane deformation and of electric fields applied perpendicular to the monolayer, i.e., along $\hat{z}$. Furthermore, we show that the presence of perpendicular electric fields may lead to the appearance of a current-induced orbital magnetization oriented parallel to the phosphorene layer.

II. DFT-DERIVED HAMILTONIAN

Phosphorene is a two-dimensional material composed of a single layer of phosphorus atoms arranged in a distorted honeycomb lattice structure [Fig. 1(a)], similar to graphene. However, unlike graphene, the lattice structure of phosphorene is puckered, with a noncoplanar configuration as illustrated in Fig. 1(b).

Our DFT calculations [36,37] were carried out with the plane-wave-based code QUANTUM ESPRESSO [38] to compute the band structure and eigenstates of phosphorene. The generalized gradient approximation (GGA) [39] was used to treat the exchange and correlation potential, while fully relativistic projector augmented wave (PAW) potentials [40,41] were employed to describe the ionic cores. To ensure accurate results, we set the wave functions' cutoff energy to 44 Ryd, and the charge density cutoff energy is ten times larger. Our self-consistent calculations (SCFs) were executed with a linear density of $\mathbf{k}$ points of $12.0\,\mathbf{k}$ points/Å^{-1} in the 2D Brillouin zone, and a minimum of 15 Å of vacuum is taken to avoid spurious interactions. We included a static electrical field (along the z direction) using a full SCF calculation via the modern theory of polarization [42].

Figure 1(c) shows the band structure of phosphorene displaying its direct band gap at the Γ point. Phosphorene's puckered crystalline structure is highly anisotropic, as evidenced by its energy spectrum near Γ, which presents a parabolic dispersion along the Γ-Y direction and a linear behavior along Γ-X. Furthermore, the puckering of the lattice has a notable impact on the mechanical and electronic characteristics of phosphorene. It renders the material more susceptible to strain, as deformation can significantly alter its band gap and electronic transport properties [28].

To perform linear response calculations, we utilized the pseudoatomic orbital projection method [43–46] implemented in the PAOFLOW code [47,48]. This approach involves constructing an effective tight-binding Hamiltonian, with no adjustable parameters, from the DFT calculations. In general, we project the plane-wave Kohn-Sham orbitals onto the compact subspace spanned by the pseudoatomic orbitals (PAOs), which are naturally included in the PAW potentials. The vast majority of cases can be accurately described by this approach with an excellent agreement between the DFT and PAOFLOW band structures. Nevertheless, occasionally the PAO basis fails to reproduce the conduction bands, especially when the unoccupied bands have a relatively strong character of an orbital that is not included in the PAO base, as in the case of phosphorene. Its conduction, and to a minor degree the valence bands, are highly hybridized with d orbitals [49]. Since the pseudopotential used in the calculation (P.rel-pbe-n-kjpaw_psl.1.0.0.UPF) is generated only with s and p orbitals, this original approach fails. To circumvent this problem, we used the recently implemented PAOFLOW internal basis, which is constructed by solving the atomic DFT problem for an all-electron configuration up to the desired orbital. Once the atomic wave function is obtained, the DFT plane-wave wave functions are projected as described in Ref. [46].

Figure 1(c) shows the effective tight binding and DFT band structure calculations superimposed. This approach significantly reduces the computational cost of performing large $\mathbf{k}$-space numerical integration. We have previously used this

method to investigate distinct characteristics of different systems, such as spin dynamics [50,51], as well as transport [52,53] and topological properties [54,55]. The orbital Hall conductivity calculations were performed with a reciprocal space sampling that is ten times larger than the one used in our DFT-SCF calculations.

III. OHE CALCULATIONS

Within linear response theory, the current density of angular momentum with polarization η, flowing along the μ direction ($\mathcal{J}_\mu^{X_\eta}$), can be generically expressed in terms of the angular momentum conductivity tensor by $\mathcal{J}_\mu^{X_\eta} = \sum_\nu \sigma_{\mu,\nu}^{X_\eta} \mathcal{E}_\nu$. Here, $\mathcal{E}_\nu$ symbolizes the ν component of the applied electric field; η, μ, and ν label the Cartesian components x, y, z. X_η represents the η component of either the orbital angular momentum operator ($\hat{\ell}_\eta$) or the spin operator ($\hat{s}_\eta$), depending on the nature of the induced angular momentum that drifts. The conductivity tensor is given by

$$\sigma_{\mu,\nu}^{X_\eta} = \frac{e}{(2\pi)^2} \sum_n \int_{\mathrm{BZ}} d^2\mathbf{k} f_{n\mathbf{k}} \Omega_{\mu,\nu,n}^{X_\eta}(\mathbf{k}), \tag{1}$$

where the orbital (spin) Berry curvature

$$\Omega_{\mu,\nu,n}^{X_\eta}(\mathbf{k}) = 2\hbar \sum_{m\neq n} \mathrm{Im}\left[\frac{\langle u_{n,\mathbf{k}} | j_{\mu,\mathbf{k}}^{X_\eta} | u_{m,\mathbf{k}} \rangle \langle u_{m,\mathbf{k}} | v_{\nu,\mathbf{k}} | u_{n,\mathbf{k}} \rangle}{(E_{n,\mathbf{k}} - E_{m,\mathbf{k}} + i0^+)^2} \right]. \tag{2}$$

The ν component of the velocity operator may be obtained by $v_{\nu,\mathbf{k}} = \hbar^{-1} \partial \mathcal{H}(\mathbf{k}) / \partial k_\nu$, where $\mathcal{H}(\mathbf{k})$ represents the Hamiltonian in reciprocal space and $\mathbf{k}$ stands for the wave vector. Here, $|u_{n,\mathbf{k}}\rangle$ is the periodic part of the Bloch eigenstate of $\mathcal{H}(\mathbf{k})$, associated with band energy $E_{n,\mathbf{k}}$, and $f_{n\mathbf{k}}$ symbolizes the Fermi-Dirac distribution function. The orbital (spin) angular momentum current operator that flows along the μ direction with orbital (spin) polarization in the η direction is defined by $j_{\mu,\mathbf{k}}^{X_\eta} = (X_\eta v_{\mu,\mathbf{k}} + v_{\mu,\mathbf{k}} X_\eta)/2$, where $X_\eta = \hat{\ell}_\eta (\hat{s}_\eta)$.

Our calculations are performed at zero temperature, but they are expected to be valid at room temperature because the energy band gap of phosphorene is relatively high (≈ 1 eV).

IV. RESULTS AND DISCUSSION

Figure 1(d) shows the orbital Hall conductivities $\sigma_{xy}^{L_z}$ and $\sigma_{yx}^{L_z}$, calculated as functions of the Fermi energy, for in-plane electric fields applied along the $\hat{y}$ and $\hat{x}$ directions, respectively. Both conductivities present a plateau inside the energy band gap. These orbital Hall conductivity plateaus are robust in the presence of disorder due to the lack of a Fermi surface in this energy region [56,57]. Phosphorene has been proposed to be a higher-order topological insulator [58,59], a type of topological state that was recently connected to the orbital Hall insulating phase [22]. We note that $\sigma_{xy}^{L_z}$ is markedly different from $\sigma_{yx}^{L_z}$ inside and close to the energy band gap, where they have opposite signs. This reflects the high anisotropy of the phosphorene lattice structure. The rectangular unit cell of phosphorene illustrated in Fig. 1(a) indicates that $\hat{x}$ and $\hat{y}$ directions are not equivalent. This is confirmed by Fig. 1(c), which shows that the valence band dispersion relations along the Γ-X and Γ-Y directions are markedly different. Hence the carrier group velocities, their effective masses, and the orbital current densities are expected to be different for electric fields applied along the $\hat{x}$ and $\hat{y}$ directions. The crystalline symmetry of phosphorene also ensures that in-plane electric fields can only induce transverse currents of angular momentum polarized along $\hat{z}$. This holds for both orbital and spin angular momentum currents, because they are subjected to essentially the same crystalline symmetry constraints [60]. In a crystal with a given space group, the spin and orbital Berry curvatures must be invariant under all symmetry operations of the group. This means that if a given symmetry operation, such as rotation, mirror reflection, or spatial inversion, changes the sign of the spin or orbital Berry curvature, then the corresponding component of the spin or orbital Hall conductivity is forbidden by symmetry. The presence or absence of symmetries in the crystal structure can dictate which components of the Hall conductivity are allowed or forbidden (see Appendix).

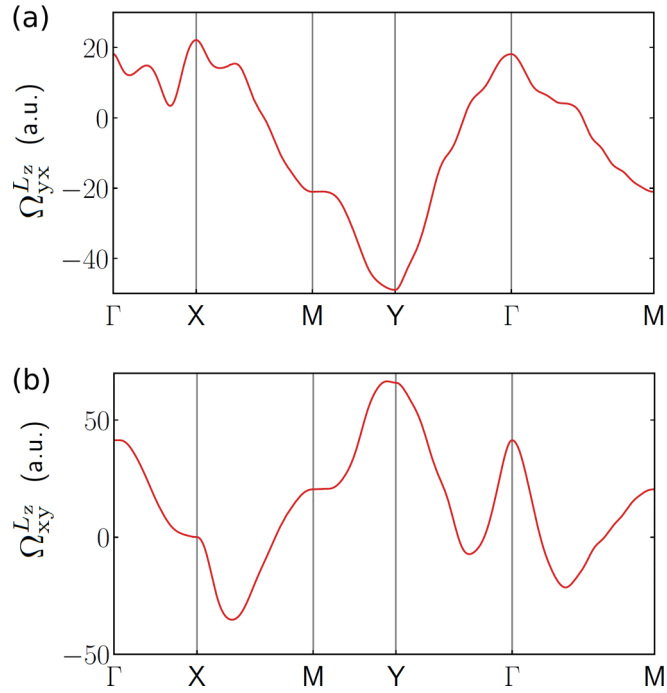

FIG. 2. Orbital Berry curvatures summed over occupied bands of phosphorene $\Omega_{yx}^{L_z}(\mathbf{k})$ (a) and $\Omega_{xy}^{L_z}(\mathbf{k})$ (b) calculated along high-symmetry directions of the Brillouin zone.

It is instructive to inquire into the regions of the 2D Brillouin zone (BZ) that contribute most to $\sigma_{xy}^{L_z}$ and $\sigma_{yx}^{L_z}$. For this purpose we have calculated the orbital Berry curvatures summed over the occupied bands of phosphorene, computed as functions of the wave vector $\mathbf{k}$ along some high-symmetry directions of the 2D BZ. The results are depicted in Fig. 2, and they clearly show that the highest contributions to both $\sigma_{xy}^{L_z}$ and $\sigma_{yx}^{L_z}$ come from the region around the Y symmetry point. Correlating the orbital Berry curvature with the band structure and the onset of the orbital Hall conductivity at energies below the gap, one can notice that the main contribution to the orbital Hall plateau originates from the transition from lower bands to the higher valence band in the region around the Y symmetry

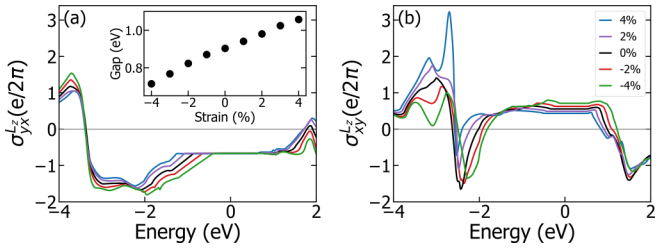

FIG. 3. Orbital Hall conductivity $\sigma_{yx}^{L_z}$ (a) and $\sigma_{xy}^{L_z}$ (b), calculated as functions of energy, for different strains (compressive and tensile) along the x axis. The inset in (a) shows the strain-induced change in the band-gap size.

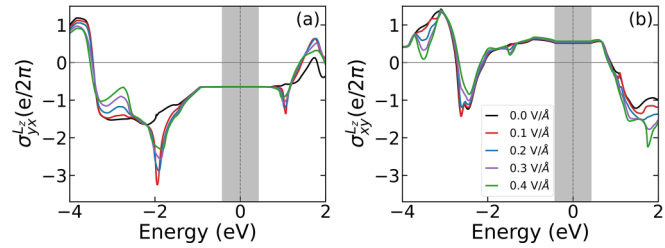

FIG. 4. Orbital Hall conductivity $\sigma_{yx}^{L_z}$ (a) and $\sigma_{xy}^{L_z}$ (b), calculated as functions of energy, for different values of the perpendicularly applied electric field $E_\perp$.

point, at energies well below the top of the valence band, which is located in Γ.

The change of sign in the phosphorene OH conductivity may be experimentally verified by observing the induced orbital magnetic moment accumulations on the boundaries of phosphorene samples, similar to SHE experiments [16,61–64]. The small spin-orbit coupling and the topological triviality of phosphorene, with respect to $\mathbb{Z}_2$, make the SHE orders of magnitude smaller than the OHE [see Fig. 1(e)]. In addition, the electronic spectrum of phosphorene has no multivalley structure in the 2D Brillouin zone and hence does not host VHE. Thus phosphorene offers an ideal platform for unambiguous observation of the OHE. We note that the OH conductivity of phosphorene is of the same order of magnitude as those predicted for monolayers of transition metal dichalcogenides [20,22]. It is noteworthy that the OHE increases with the number of layers [23,24,65], and so, thin films of black phosphorus may be employed to enhance the OH signal in such experiments. However, one must keep in mind that the band gap decreases monotonically with the increase in the number of layers, saturating at approximately 0.3 eV for sufficiently large film thicknesses [32].

In general, the transport properties of 2D materials are influenced by the substrate, which may cause strain and/or alter the features of the sample's surface in contact with it. In some cases it is necessary to encapsulate the film to prevent its deterioration from oxidation and also be able to control its density of carriers with gate voltages. Therefore it is worth investigating how strain and the presence of an auxiliary perpendicular electric field would affect the orbital transport properties of phosphorene.

A. Effects of strain

Figure 3 illustrates the effects of uniaxial strain (both compressive and tensile) along the $\hat{x}$ direction, on the OH conductivity (OHC) components $\sigma_{xy}^{L_z}$ and $\sigma_{yx}^{L_z}$.

When subjected to moderate in-plane uniform strain, the unit cell of phosphorene maintains its rectangular shape, as long as it does not undergo structural phase transitions, which typically require high levels of strain [66,67]. Thus, with the values of strain used in Fig. 3, the D_{2h} group symmetry of phosphorene is preserved, and hence only the L_z component of the OHC remains non-null. Strain clearly affects the OH conductivity of phosphorene. It modifies the electronic states around the band gap [68] and may alter their orbital features and the orbital transport in general. It is noteworthy that the plateau heights of $\sigma_{xy}^{L_z}$ and $\sigma_{yx}^{L_z}$ do not change significantly under moderate deformations along the x direction, showing that the OHE is reasonably robust to uniaxial strain within the energy band gap of phosphorene. On the other hand, the lengths of the OHC plateaus decrease (increase) under compressive (tensile) strain, which is expected because the energy band-gap size follows the same trend [69], as illustrated in the inset of Fig. 3(a).

B. Effect of perpendicular electric field

1. *Orbital Hall conductivity*

We shall now examine how the OHC of phosphorene is affected by an electric field $\vec{E}_\perp = E_\perp \hat{z}$, applied perpendicularly to its layer. The presence of $\vec{E}_\perp$ reduces the phosphorene point group D_{2h} to C_{2v}, which belong to the same Laue class *mmm*. Since the Laue class determines the general form of the OHC tensor [70,71], only the L_z component of the OHC remains non-null in the presence of the $\vec{E}_\perp$ (see Appendix).

Figure 4 shows $\sigma_{yx}^{L_z}$ and $\sigma_{xy}^{L_z}$, calculated as functions of energy, for different values of $E_\perp$. We note that the OHC is much more affected by $E_\perp$ in some energy ranges outside the band gap than within it. We recall that ultrathin films of black phosphorus can switch to a topological insulating phase for sufficiently high values of $E_\perp$, as discussed in Ref. [32]. However, for phosphorene, this phase transition requires values of $E_\perp \gg 0.6\,\mathrm{V/m}$, which is higher than the ones considered in Fig. 4.

2. *Orbital magnetoelectric effect*

The noncentrosymmetric and polar C_{2v} point group allows the occurrence of the orbital magnetoelectric effect (OME) mediated by Fermi-surface conducting states [65,72–76]. The perpendicular electric field $\vec{E}_\perp$ distorts the phosphorene's charge distribution, giving rise to a finite polarization $\vec{P} = P_z \hat{z}$ perpendicular to its layer [35]. The driving field in the phosphorene plane exerts a torque on the electric dipoles, thereby inducing a net orbital magnetization $\vec{M}^L \propto \vec{P} \times \vec{\mathcal{E}}$ [65,73,77,78]. One may calculate $\vec{M}^L$ utilizing a scheme similar to the one described in Secs. II and III. Since time-reversal symmetry is preserved, there are no interband contributions to the orbital magnetoelectric effect in phosphorene. Thus, to first order in the in-plane driving field and for finite values of $E_\perp$, the current-induced orbital magnetization per unit cell area of phosphorene is given by $m_{L_\eta} = \sum_\nu \alpha_{\eta\nu} \mathcal{E}_\nu$ [79,80],

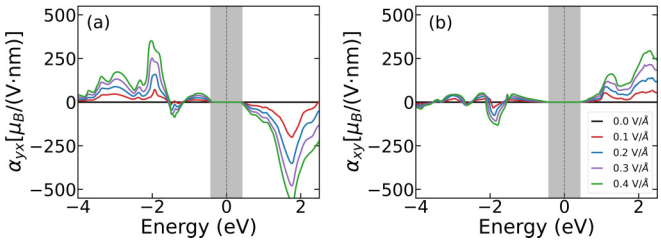

FIG. 5. Orbital magnetoelectric coefficients α_{yx} (a) and α_{xy} (b), calculated as functions of energy, for different values of the perpendicularly applied electric field $E_\perp$.

where

$$\alpha_{\eta\nu} = \frac{e\mu_B}{2\Gamma}\sum_n \int_{\mathrm{BZ}} \frac{d^2\mathbf{k}}{(2\pi)^2}\frac{\partial f_{n,\mathbf{k}}}{\partial E} \times \langle u_{n,\mathbf{k}}|\, v_{\nu,\mathbf{k}}\, |u_{n,\mathbf{k}}\rangle \langle u_{n,\mathbf{k}}|\, \hat{\ell}_\eta\, |u_{n,\mathbf{k}}\rangle \tag{3}$$

represents the matrix elements of the magnetoelectric tensor. Here, μ_B is the Bohr magneton, and Γ is the energy scale associated with the electronic relaxation time $\tau_e = \hbar/2\Gamma$. This phenomenological parameter simulates effects of scattering by inhomogeneities and thermal effects due to phonons. In our calculations we have used $\Gamma = 1.6$ meV, which corresponds to $\tau_e \approx 200$ fs [34]. Figure 5 shows α_{xy} and α_{yx} calculated as functions of energy for different values of $E_\perp$. As expected, the OME clearly vanishes within the band-gap energy range. However, in the conductive regime, it can reach sizable values for both m_{L_y} and m_{L_x}, in response to electric fields applied along the $\hat{x}$ and $\hat{y}$ directions, respectively. This in-plane-induced orbital magnetization adds up to the orbital angular momenta accumulated at the sample's edges, due to the OHE, transforming its original antiferromagneticlike disposition into a noncollinear orbital magnetic arrangement.

In some energy ranges the OME varies appreciably with $E_\perp$, which may be used to control the OME intensity. In order to roughly estimate the order of magnitude of the in-plane OME, we consider an electric field with intensity $\mathcal{E}_x = 10^5$ V/m and a carrier density that leads to $\alpha_{yx} = -2 \times 10^2\, \mu_B/(\mathrm{V\,nm})$. In this case, the induced orbital magnetization $m_{L_y} \approx -0.3 \times 10^{-2}\, \mu_B/A_{\mathrm{u.c.}}$, where $A_{\mathrm{u.c.}} = 0.152\,\mathrm{nm}^2$ represents the phosphorene unit cell area. This has the same order of magnitude as the Edelstein effect estimated for Bi/Ag(111) in Ref. [81] assuming a larger value of τ_e.

V. FINAL REMARKS AND CONCLUSIONS

To summarize, we argue that thin films of black phosphorus may provide suitable 2D platforms for direct observation of the orbital Hall effect. To this end, we combine linear response theory with density functional theory calculations to investigate the orbital conductivity of phosphorene and explore how it is affected by uniform strain and perpendicular electric fields. We show that phosphorene displays a fairly large OHC, with perpendicular orbital polarization, which is orders of magnitude larger than the spin Hall conductivity (SHC). This OHC is also highly anisotropic with respect to the direction of the in-plane applied electric field, and may even switch sign when the driving field direction is changed. Inside the energy band gap, it exhibits an orbital Hall insulating plateau that is robust under moderate uniform strain and perpendicular electric fields. The latter breaks spatial-inversion symmetry and may lead to the appearance of an in-plane orbital magnetization, induced by an in-plane electric current. This effect alters the antisymmetric profile of the orbital magnetic moment induced by the orbital Hall effect in the conducting phase. Our numerical calculations are complemented by symmetry analysis.

ACKNOWLEDGMENTS

We acknowledge CNPq (Brazil); CAPES (Brazil), FAPERJ (Brazil), INCT Nanocarbono, and INCT Materials Informatics for financial support. T.G.R. acknowledges funding from FCT-Portugal through Grant No. CEECIND/07471/2022. She thankfully acknowledges the computer resources at MareNostrum and the technical support provided by Barcelona Supercomputing Center (FI-2020-2-0033). M.C. acknowledges CNPq (Grant No. 317320/2021-1) and FAPERJ (Grant No. E26/200.240/2023). We thank Prof. A. Fazzio and Prof. P. Venezuela for fruitful discussions. We also thank Professor Davide Ceresoli for implementing the PAOFLOW internal basis.

APPENDIX A: SYMMETRY CONSTRAINT ON ORBITAL HALL CONDUCTIVITY

The crystal symmetry operations of phosphorene are E, $\tau\mathcal{C}_{2x}$, $\mathcal{C}_{2y}$, $\tau\mathcal{C}_{2z}$, $\mathcal{P}$, $\tau\mathcal{M}_x$, $\mathcal{M}_y$, and $\tau\mathcal{M}_z$ [27]. Here, E represents the identity operation, $\mathcal{C}_{2\mu}$ is a 180° rotation around the μ axis, $\mathcal{M}_\mu$ denotes a reflection through a mirror plane that is perpendicular to the μ axis, and $\mathcal{P}$ symbolizes the spatial-inversion operation; $\tau\mathcal{O}$ designates the action of $\mathcal{O}$ followed by a half-unit-cell translation $\vec{\tau} = (a_x/2, a_y/2)$, where a_x and a_y represent the moduli of the unit cell lattice vectors. This set of symmetries is isomorphic to the point group $D_{2\mathrm{h}}$, which correspond to Laue group *mmm* [70]. Consequently, for a phosphorene layer in the xy plane, only the L_z component of the OHE is allowed [71]. It is possible to derive the constraints to the OH conductivity tensor imposed by each symmetry operation of phosphorene. They are summarized in Table I.

TABLE I. Constraints on the OHC of phosphorene imposed by crystal symmetry. We assume that the phosphorene layer lies in the xy plane, with the $\hat{x}$ and $\hat{y}$ axes oriented as illustrated in Fig. 1. The constraints hold for both $\sigma_{xy}^{L_\eta}$ and $\sigma_{yx}^{L_\eta}$, which are generically represented here by $\sigma_{\mathrm{OH}}^{L_\eta}$. The OHC components that are allowed (forbidden) by symmetry are identified by ◯ (×).

Symmetry	$\sigma_{\mathrm{OH}}^{L_x}$	$\sigma_{\mathrm{OH}}^{L_y}$	$\sigma_{\mathrm{OH}}^{L_z}$
$\mathcal{P}$	◯	◯	◯
$\tau\mathcal{M}_z$, $\tau\mathcal{C}_{2z}$[a]	×	×	◯
$\tau\mathcal{M}_x$,[a] $\tau\mathcal{C}_{2x}$	×	◯	◯
$\mathcal{M}_y$,[a] $\mathcal{C}_{2y}$	◯	×	◯

[a]A crystal symmetry operation of phosphorene in the presence of $\vec{E}_\perp$.

TABLE II. Signs of the velocity and OAM operator component acquired when transformed under the symmorphic part $\mathcal{O}$ of operations associated with the D_{2h} point group of phosphorene. This table can be used to determine the allowed components of the OHC tensor presented in Table I.

Symmetry	$s_{\mathcal{O},v_x}$	$s_{\mathcal{O},v_y}$	$s_{\mathcal{O},L_x}$	$s_{\mathcal{O},L_y}$	$s_{\mathcal{O},L_z}$
$\mathcal{P}$	-1	-1	$+1$	$+1$	$+1$
$\mathcal{M}_z$	$+1$	$+1$	-1	-1	$+1$
$\mathcal{M}_x$	-1	$+1$	$+1$	-1	-1
$\mathcal{M}_y$	$+1$	-1	-1	$+1$	-1
$\mathcal{C}_{2z}$	-1	-1	-1	-1	$+1$
$\mathcal{C}_{2x}$	$+1$	-1	$+1$	-1	-1
$\mathcal{C}_{2y}$	-1	$+1$	-1	$+1$	-1

In the presence of $\vec{E}_\perp$ all symmetry operations that interchange z and $-z$ are excluded, leaving just $\tau\mathcal{C}_{2z}$, $\tau\mathcal{M}_x$, $\mathcal{M}_y$, and E, which are identified with a footnote in Table I. In this case, the point group is reduced from D_{2h} to C_{2v}. However, since C_{2v} and D_{2h} belong to the same Laue class (*mmm*), only the L_z component of the OHC can be nonzero when phosphorene is subjected to $\vec{E}_\perp$ [70,71].

In order to obtain the constraints on the OHC components presented in Table I, we consider the action of $\tau\mathcal{O}$ on the Bloch eigenstates $\psi_{n,\mathbf{k}}(\mathbf{r})$ associated with the eigenvalue $E_{n,\mathbf{k}}$, namely, $\tau\mathcal{O}\psi_{n,\mathbf{k}}(\mathbf{r}) = \exp(-i\vec{\tau}\cdot\mathbf{k})\psi_{n,\mathcal{O}\mathbf{k}}(\mathbf{r})$ [82]. Since the Hamiltonian is invariant under $\tau\mathcal{O}$, $E_{n,\mathbf{k}} = E_{n,\mathcal{O}\mathbf{k}}$.

Let us examine, for example, $\Omega^{L_\eta}_{yx,n}(\mathbf{k})$. Inserting the identity $(\tau\mathcal{O})^\dagger(\tau\mathcal{O}) = \mathbb{1}$ into the orbital-weighted Berry curvature and using the above relations, we obtain

$$\Omega^{L_\eta}_{yx,n}(\mathbf{k}) = 2\hbar\sum_{m\neq n}\mathrm{Im}\left[\frac{\langle u_{n,\mathbf{k}}|(\tau\mathcal{O})^\dagger(\tau\mathcal{O})j^{L_\eta}_{y,\mathbf{k}}(\tau\mathcal{O})^\dagger(\tau\mathcal{O})|u_{m,\mathbf{k}}\rangle\langle u_{m,\mathbf{k}}|(\tau\mathcal{O})^\dagger(\tau\mathcal{O})v_{x,\mathbf{k}}(\tau\mathcal{O})^\dagger(\tau\mathcal{O})|u_{n,\mathbf{k}}\rangle}{(E_{n,\mathbf{k}}-E_{m,\mathbf{k}}+i0^+)^2}\right]. \tag{A1}$$

The restrictions on the conductivity tensor depend on how the Cartesian components of the velocity and angular momentum operators transform under the group symmetry operations. This information is contained in its character table, which shows that, for the point group of phosphorene, they only acquire a sign $s_{\mathcal{O},\hat{A}} = \pm 1$ [27] under such operations, as Table II illustrates. Therefore

$$\begin{aligned}\Omega^{L_\eta}_{yx,n}(\mathbf{k}) &= 2\hbar\sum_{m\neq n}\mathrm{Im}\left[\frac{\langle u_{n,\mathcal{O}\mathbf{k}}|s_{\mathcal{O},\hat{v}_y}s_{\mathcal{O},\hat{L}_\eta}j^{L_\eta}_{y,\mathcal{O}\mathbf{k}}|u_{m,\mathcal{O}\mathbf{k}}\rangle\langle u_{m,\mathcal{O}\mathbf{k}}|s_{\mathcal{O},\hat{v}_x}v_{x,\mathcal{O}\mathbf{k}}|u_{n,\mathcal{O}\mathbf{k}}\rangle}{(E_{n,\mathcal{O}\mathbf{k}}-E_{m,\mathcal{O}\mathbf{k}}+i0^+)^2}\right]\\ &= s_{\mathcal{O},\hat{v}_x}s_{\mathcal{O},\hat{v}_y}s_{\mathcal{O},\hat{L}_\eta}\Omega^{L_\eta}_{yx,n}(\mathcal{O}\mathbf{k}).\end{aligned} \tag{A2}$$

The same expression holds for $\Omega^{L_\eta}_{xy,n}(\mathbf{k})$.

Since $\int d^2\mathbf{k} = \int d^2(\mathcal{O}\mathbf{k})$, it follows from Eq. (1) that

$$\mathcal{O}: \quad \sigma^{L_\eta}_{\mathrm{OH}} = \bar{s}^\eta_{\mathrm{OH}}(\mathcal{O})\sigma^{L_\eta}_{\mathrm{OH}}, \tag{A3}$$

where $\bar{s}^\eta_{\mathrm{OH}}(\mathcal{O}) = s_{\mathcal{O},v_x}\times s_{\mathcal{O},v_y}\times s_{\mathcal{O},L_\eta}$. If $\bar{s}^\eta_{\mathrm{OH}}(\mathcal{O}) = +1$, the symmetry $\mathcal{O}$ does not impose a constraint on the OH conductivity. However, if $\bar{s}^\eta_{\mathrm{OH}}(\mathcal{O}) = -1$, $\sigma^{L_\eta}_{\mathrm{OH}} = 0$.

[1] B. A. Bernevig, T. L. Hughes, and S.-C. Zhang, Orbitronics: The intrinsic orbital current in *p*-doped silicon, Phys. Rev. Lett. **95**, 066601 (2005).

[2] V. o. T. Phong, Z. Addison, S. Ahn, H. Min, R. Agarwal, and E. J. Mele, Optically controlled orbitronics on a triangular lattice, Phys. Rev. Lett. **123**, 236403 (2019).

[3] L. Salemi and P. M. Oppeneer, First-principles theory of intrinsic spin and orbital Hall and nernst effects in metallic monoatomic crystals, Phys. Rev. Mater. **6**, 095001 (2022).

[4] L. Salemi and P. M. Oppeneer, Theory of magnetic spin and orbital Hall and Nernst effects in bulk ferromagnets, Phys. Rev. B **106**, 024410 (2022).

[5] A. Bose, F. Kammerbauer, R. Gupta, D. Go, Y. Mokrousov, G. Jakob, and M. Kläui, Detection of long-range orbital-Hall torques, Phys. Rev. B **107**, 134423 (2023).

[6] G. Go, D. An, H.-W. Lee, and S. K. Kim, Intrinsic magnon orbital Hall effect in honeycomb antiferromagnets, arXiv:2303.11687.

[7] M. Zeer, D. Go, J. P. Carbone, T. G. Saunderson, M. Redies, M. Kläui, J. Ghabboun, W. Wulfhekel, S. Blügel, and Y. Mokrousov, Spin and orbital transport in rare-earth dichalcogenides: The case of EuS_2, Phys. Rev. Mater. **6**, 074004 (2022).

[8] S. Han, H.-W. Lee, and K.-W. Kim, Orbital dynamics in centrosymmetric systems, Phys. Rev. Lett. **128**, 176601 (2022).

[9] D. B. Fonseca, L. L. A. Pereira, and A. L. R. Barbosa, Orbital Hall effect in mesoscopic devices, arXiv:2305.01640.

[10] G. Sala and P. Gambardella, Giant orbital Hall effect and orbital-to-spin conversion in $3d$, $5d$, and $4f$ metallic heterostructures, Phys. Rev. Res. **4**, 033037 (2022).

[11] S. Urazhdin, Symmetry constraints on the orbital transport in solids, arXiv:2309.04442.

[12] O. Busch, I. Mertig, and B. Göbel, Orbital Hall effect and orbital edge states caused by s electrons, Phys. Rev. Res. **5**, 043052 (2023).

[13] S. L. M., J. Henk, I. Mertig, and A. Johansson, Spin and orbital Edelstein effect in a bilayer system with Rashba interaction, arXiv:2307.02872.

[14] D. Go, D. Jo, C. Kim, and H.-W. Lee, Intrinsic spin and orbital Hall effects from orbital texture, Phys. Rev. Lett. **121**, 086602 (2018).

[15] D. Go, D. Jo, H.-W. Lee, M. Kläui, and Y. Mokrousov, Orbitronics: Orbital currents in solids, Europhys. Lett. **135**, 37001 (2021).

[16] Y.-G. Choi, D. Jo, K.-H. Ko, D. Go, K.-H. Kim, H. G. Park, C. Kim, B.-C. Min, G.-M. Choi, and H.-W. Lee, Observation of the orbital Hall effect in a light metal Ti, Nature (London) **619**, 52 (2023).

[17] Z. C. Zheng, Q. X. Guo, D. Jo, D. Go, L. H. Wang, H. C. Chen, W. Yin, X. M. Wang, G. H. Yu, W. He, H.-W. Lee, J. Teng, and T. Zhu, Magnetization switching driven by current-induced torque from weakly spin-orbit coupled Zr, Phys. Rev. Res. **2**, 013127 (2020).

[18] S. Lee, M.-G. Kang, D. Go, D. Kim, J.-H. Kang, T. Lee, G.-H. Lee, J. Kang, N. J. Lee, Y. Mokrousov, S. Kim, K.-J. Kim, K.-J. Lee, and B.-G. Park, Efficient conversion of orbital Hall current to spin current for spin-orbit torque switching, Commun. Phys. **4**, 234 (2021).

[19] D. Lee, D. Go, H.-J. Park, W. Jeong, H.-W. Ko, D. Yun, D. Jo, S. Lee, G. Go, J. H. Oh, K.-J. Kim, B.-G. Park, B.-C. Min, H. C. Koo, H.-W. Lee, O. Lee, and K.-J. Lee, Orbital torque in magnetic bilayers, Nat. Commun. **12**, 6710 (2021).

[20] L. M. Canonico, T. P. Cysne, A. Molina-Sanchez, R. B. Muniz, and T. G. Rappoport, Orbital Hall insulating phase in transition metal dichalcogenide monolayers, Phys. Rev. B **101**, 161409(R) (2020).

[21] L. M. Canonico, T. P. Cysne, T. G. Rappoport, and R. B. Muniz, Two-dimensional orbital Hall insulators, Phys. Rev. B **101**, 075429 (2020).

[22] M. Costa, B. Focassio, L. M. Canonico, T. P. Cysne, G. R. Schleder, R. B. Muniz, A. Fazzio, and T. G. Rappoport, Connecting higher-order topology with the orbital Hall effect in monolayers of transition metal dichalcogenides, Phys. Rev. Lett. **130**, 116204 (2023).

[23] T. P. Cysne, M. Costa, L. M. Canonico, M. B. Nardelli, R. B. Muniz, and T. G. Rappoport, Disentangling orbital and valley Hall effects in bilayers of transition metal dichalcogenides, Phys. Rev. Lett. **126**, 056601 (2021).

[24] T. P. Cysne, S. Bhowal, G. Vignale, and T. G. Rappoport, Orbital Hall effect in bilayer transition metal dichalcogenides: From the intra-atomic approximation to the Bloch states orbital magnetic moment approach, Phys. Rev. B **105**, 195421 (2022).

[25] S. Bhowal and G. Vignale, Orbital Hall effect as an alternative to valley Hall effect in gapped graphene, Phys. Rev. B **103**, 195309 (2021).

[26] J. Salvador-Sánchez, L. M. Canonico, A. Pérez-Rodríguez, T. P. Cysne, Y. Baba, V. Clericò, M. Vila, D. Vaquero, J. A. Delgado-Notario, J. M. Caridad, K. Watanabe, T. Taniguchi, R. A. Molina, F. Domínguez-Adame, S. Roche, E. Diez, T. G. Rappoport, and M. Amado, Generation and control of non-local chiral currents in graphene superlattices by orbital Hall effect, arXiv:2206.04565.

[27] P. Li and I. Appelbaum, Electrons and holes in phosphorene, Phys. Rev. B **90**, 115439 (2014).

[28] A. S. Rodin, A. Carvalho, and A. H. Castro Neto, Strain-induced gap modification in black phosphorus, Phys. Rev. Lett. **112**, 176801 (2014).

[29] E. Taghizadeh Sisakht, F. Fazileh, M. H. Zare, M. Zarenia, and F. M. Peeters, Strain-induced topological phase transition in phosphorene and in phosphorene nanoribbons, Phys. Rev. B **94**, 085417 (2016).

[30] A. N. Rudenko and M. I. Katsnelson, Quasiparticle band structure and tight-binding model for single- and bilayer black phosphorus, Phys. Rev. B **89**, 201408 (2014).

[31] P. E. Faria Junior, M. Kurpas, M. Gmitra, and J. Fabian, $k \cdot p$ theory for phosphorene: Effective g-factors, Landau levels, and excitons, Phys. Rev. B **100**, 115203 (2019).

[32] Q. Liu, X. Zhang, L. B. Abdalla, A. Fazzio, and A. Zunger, Switching a normal insulator into a topological insulator via electric field with application to phosphorene, Nano Lett. **15**, 1222 (2015).

[33] Z. S. Popović, J. M. Kurdestany, and S. Satpathy, Electronic structure and anisotropic Rashba spin-orbit coupling in monolayer black phosphorus, Phys. Rev. B **92**, 035135 (2015).

[34] A. Avsar, J. Y. Tan, M. Kurpas, M. Gmitra, K. Watanabe, T. Taniguchi, J. Fabian, and B. Özyilmaz, Gate-tunable black phosphorus spin valve with nanosecond spin lifetimes, Nat. Phys. **13**, 888 (2017).

[35] T. Hu, H. Wu, H. Zeng, K. Deng, and E. Kan, New ferroelectric phase in atomic-thick phosphorene nanoribbons: Existence of in-plane electric polarization, Nano Lett. **16**, 8015 (2016).

[36] P. Hohenberg and W. Kohn, Inhomogeneous electron gas, Phys. Rev. **136**, B864 (1964).

[37] W. Kohn and L. J. Sham, Self-consistent equations including exchange and correlation effects, Phys. Rev. **140**, A1133 (1965).

[38] P. Giannozzi, O. Andreussi, T. Brumme, O. Bunau, M. Buongiorno Nardelli, M. Calandra, R. Car, C. Cavazzoni, D. Ceresoli, M. Cococcioni, N. Colonna, I. Carnimeo, A. D. Corso, S. de Gironcoli, P. Delugas, R. A. DiStasio Jr, A. Ferretti, A. Floris, G. Fratesi, G. Fugallo *et al.*, Advanced capabilities for materials modelling with QUANTUM ESPRESSO, J. Phys.: Condens. Matter **29**, 465901 (2017).

[39] J. P. Perdew, K. Burke, and M. Ernzerhof, Generalized gradient approximation made simple, Phys. Rev. Lett. **77**, 3865 (1996).

[40] G. Kresse and D. Joubert, From ultrasoft pseudopotentials to the projector augmented-wave method, Phys. Rev. B **59**, 1758 (1999).

[41] A. Dal Corso, Pseudopotentials periodic table: From H to Pu, Comput. Mater. Sci. **95**, 337 (2014).

[42] T. Brumme, M. Calandra, and F. Mauri, First-principles theory of field-effect doping in transition-metal dichalcogenides: Structural properties, electronic structure, Hall coefficient, and electrical conductivity, Phys. Rev. B **91**, 155436 (2015).

[43] L. A. Agapito, A. Ferretti, A. Calzolari, S. Curtarolo, and M. Buongiorno Nardelli, Effective and accurate representation of extended Bloch states on finite Hilbert spaces, Phys. Rev. B **88**, 165127 (2013).

[44] L. A. Agapito, S. Curtarolo, and M. Buongiorno Nardelli, Reformulation of DFT+U as a pseudohybrid Hubbard density

functional for accelerated materials discovery, Phys. Rev. X **5**, 011006 (2015).
[45] L. A. Agapito, M. Fornari, D. Ceresoli, A. Ferretti, S. Curtarolo, and M. B. Nardelli, Accurate tight-binding Hamiltonians for two-dimensional and layered materials, Phys. Rev. B **93**, 125137 (2016).
[46] L. A. Agapito, S. Ismail-Beigi, S. Curtarolo, M. Fornari, and M. B. Nardelli, Accurate tight-binding Hamiltonian matrices from *ab initio* calculations: Minimal basis sets, Phys. Rev. B **93**, 035104 (2016).
[47] M. Buongiorno Nardelli, F. T. Cerasoli, M. Costa, S. Curtarolo, R. D. Gennaro, M. Fornari, L. Liyanage, A. R. Supka, and H. Wang, PAOFLOW: A utility to construct and operate on *ab initio* Hamiltonians from the projections of electronic wavefunctions on atomic orbital bases, including characterization of topological materials, Comput. Mater. Sci. **143**, 462 (2018).
[48] F. T. Cerasoli, A. R. Supka, A. Jayaraj, M. Costa, I. Siloi, J. Sławińska, S. Curtarolo, M. Fornari, D. Ceresoli, and M. B. Nardelli, Advanced modeling of materials with PAOFLOW 2.0: New features and software design, Comput. Mater. Sci. **200**, 110828 (2021).
[49] M. G. Menezes and R. B. Capaz, Tight binding parametrization of few-layer black phosphorus from first-principles calculations, Comput. Mater. Sci. **143**, 411 (2018).
[50] M. Costa, M. B. Nardelli, A. Fazzio, and A. T. Costa, Long range dynamical coupling between magnetic adatoms mediated by a 2D topological insulator, arXiv:1808.00347.
[51] M. Costa, N. M. R. Peres, J. Fernández-Rossier, and A. T. Costa, Nonreciprocal magnons in a two-dimensional crystal with out-of-plane magnetization, Phys. Rev. B **102**, 014450 (2020).
[52] M. Costa, G. R. Schleder, C. M. Acosta, A. C. M. Padilha, F. Cerasoli, M. B. Nardelli, and A. Fazzio, Discovery of higher-order topological insulators using the spin Hall conductivity as a topology signature, npj Comput. Mater. **7**, 49 (2021).
[53] J. J. Heath, M. Costa, M. Buongiorno-Nardelli, and M. A. Kuroda, Role of quantum confinement and interlayer coupling in CrI_3-graphene magnetic tunnel junctions, Phys. Rev. B **101**, 195439 (2020).
[54] M. Costa, G. R. Schleder, M. Buongiorno Nardelli, C. Lewenkopf, and A. Fazzio, Toward realistic amorphous topological insulators, Nano Lett. **19**, 8941 (2019).
[55] M. Costa, A. T. Costa, W. A. Freitas, T. M. Schmidt, M. Buongiorno Nardelli, and A. Fazzio, Controlling topological states in topological/normal insulator heterostructures, ACS Omega **3**, 15900 (2018).
[56] H. Liu and D. Culcer, Dominance of extrinsic scattering mechanisms in the orbital Hall effect: graphene, transition metal dichalcogenides and topological antiferromagnets, arXiv:2308.14878.
[57] O. V. Dimitrova, Spin-Hall conductivity in a two-dimensional Rashba electron gas, Phys. Rev. B **71**, 245327 (2005).
[58] M. Hitomi, T. Kawakami, and M. Koshino, Multiorbital edge and corner states in black phosphorene, Phys. Rev. B **104**, 125302 (2021).
[59] M. Ezawa, Minimal models for Wannier-type higher-order topological insulators and phosphorene, Phys. Rev. B **98**, 045125 (2018).
[60] H. Lee, B. Choi, and H.-W. Lee, Orientational dependence of intrinsic orbital and spin Hall effects in hcp structure materials, Phys. Rev. B **105**, 035142 (2022).
[61] T. Jungwirth, J. Wunderlich, and K. Olejník, Spin Hall effect devices, Nat. Mater. **11**, 382 (2012).
[62] Y. Marui, M. Kawaguchi, S. Sumi, H. Awano, K. Nakamura, and M. Hayashi, Spin and orbital Hall currents detected via current induced magneto-optical Kerr effect in V and Pt, arXiv:2306.09585.
[63] S. Kumar and S. Kumar, Ultrafast THz probing of nonlocal orbital current in transverse multilayer metallic heterostructures, arXiv:2306.17027.
[64] I. Lyalin, S. Alikhah, M. Berritta, P. M. Oppeneer, and R. K. Kawakami, Magneto-optical detection of the orbital Hall effect in chromium, Phys. Rev. Lett. **131**, 156702 (2023).
[65] T. P. Cysne, F. S. M. Guimarães, L. M. Canonico, M. Costa, T. G. Rappoport, and R. B. Muniz, Orbital magnetoelectric effect in nanoribbons of transition metal dichalcogenides, Phys. Rev. B **107**, 115402 (2023).
[66] J. Ribeiro-Soares, R. M. Almeida, L. G. Cançado, M. S. Dresselhaus, and A. Jorio, Group theory for structural analysis and lattice vibrations in phosphorene systems, Phys. Rev. B **91**, 205421 (2015).
[67] T. Hu and J. Dong, Structural phase transitions of phosphorene induced by applied strains, Phys. Rev. B **92**, 064114 (2015).
[68] X. Peng, Q. Wei, and A. Copple, Strain-engineered direct-indirect band gap transition and its mechanism in two-dimensional phosphorene, Phys. Rev. B **90**, 085402 (2014).
[69] D. Midtvedt, C. H. Lewenkopf, and A. Croy, Strain–displacement relations for strain engineering in single-layer 2d materials, 2D Mater. **3**, 011005 (2016).
[70] M. Seemann, D. Ködderitzsch, S. Wimmer, and H. Ebert, Symmetry-imposed shape of linear response tensors, Phys. Rev. B **92**, 155138 (2015).
[71] A. Roy, M. H. D. Guimarães, and J. Sławińska, Unconventional spin Hall effects in nonmagnetic solids, Phys. Rev. Mater. **6**, 045004 (2022).
[72] T. Furukawa, Y. Watanabe, N. Ogasawara, K. Kobayashi, and T. Itou, Current-induced magnetization caused by crystal chirality in nonmagnetic elemental tellurium, Phys. Rev. Res. **3**, 023111 (2021).
[73] T. P. Cysne, F. S. M. Guimarães, L. M. Canonico, T. G. Rappoport, and R. B. Muniz, Orbital magnetoelectric effect in zigzag nanoribbons of *p*-band systems, Phys. Rev. B **104**, 165403 (2021).
[74] K. Shinada and R. Peters, Orbital gravitomagnetoelectric response and orbital magnetic quadrupole moment correction, Phys. Rev. B **107**, 214109 (2023).
[75] K. Shinada, A. Kofuji, and R. Peters, Quantum theory of the intrinsic orbital magnetoelectric effect in itinerant electron systems at finite temperatures, Phys. Rev. B **107**, 094106 (2023).
[76] S. Hayami, M. Yatsushiro, Y. Yanagi, and H. Kusunose, Classification of atomic-scale multipoles under crystallographic point groups and application to linear response tensors, Phys. Rev. B **98**, 165110 (2018).
[77] S. Hayami, H. Kusunose, and Y. Motome, Emergent spin-valley-orbital physics by spontaneous parity breaking, J. Phys.: Condens. Matter **28**, 395601 (2016).

[78] L. Salemi, M. Berritta, A. K. Nandy, and P. M. Oppeneer, Orbitally dominated Rashba-Edelstein effect in noncentrosymmetric antiferromagnets, Nat. Commun. **10**, 5381 (2019).

[79] T. Yoda, T. Yokoyama, and S. Murakami, Orbital Edelstein effect as a condensed-matter analog of solenoids, Nano Lett. **18**, 916 (2018).

[80] W.-Y. He, D. Goldhaber-Gordon, and K. T. Law, Giant orbital magnetoelectric effect and current-induced magnetization switching in twisted bilayer graphene, Nat. Commun. **11**, 1650 (2020).

[81] A. Johansson, J. Henk, and I. Mertig, Edelstein effect in Weyl semimetals, Phys. Rev. B **97**, 085417 (2018).

[82] M. Dresselhaus, G. Dresselhaus, and A. Jorio, *Group Theory: Application to the Physics of Condensed Matter* (Springer, Berlin, 2007).